Supplementary materials

Enhancement of average thermoelectric figure of merit by increasing the grain-size of $Mg_{3.2}Sb_{1.5}Bi_{0.49}Te_{0.01}$

Tsutomu Kanno,[1,a)] Hiromasa Tamaki,[1] Hiroki K. Sato,[1] Stephen Dongmin Kang,[2,3] Saneyuki Ohno,[2,3,4] Kazuki Imasato,[2] Jimmy Jiahong Kuo,[2] G. Jeffrey Snyder,[2] and Yuzuru Miyazaki[5]

[1]Advanced Research Division, Panasonic Corporation, Seika, Kyoto 619-0237, Japan

[2]Department of Materials Science and Engineering, Northwestern University, Evanston, Illinois 60208, USA

[3]Department of Applied Physics and Materials Science, California Institute of Technology, Pasadena, CA 91125, USA

[4]Institute of Physical Chemistry, Justus-Liebig-University Giessen, Heinrich-Buff-Ring 17, 35392 Giessen, Germany

[5]Department of Applied Physics, Tohoku University, Sendai, Miyagi 980-8579, Japan.

[a)]Corresponding author: kanno.tsutomu@jp.panasonic.com

S1. Crystal structure refinement

S2. Electron backscattering diffraction (EBSD) mapping

S3. Chemical composition analysis

S4. Thermal stability

S1. Crystal structure refinement

Synchrotron X-ray diffraction (XRD) measurement of a powder sample was performed at the 11-BM beamline of the Advanced Photon Source (APS) in USA. The sample was prepared with the nominal composition of $Mg_{3.2}Sb_{1.5}Bi_{0.49}Te_{0.01}$ and the hot-press temperature was 873 K. The Rietveld refinement was performed using the GSAS-II program.[1] The Thompson-Cox-Hastings pseudo-Voigt function [2] was used for a profile function. The anisotropic profile broadening was refined using the phenomenological model by Stephens.[3] The background was refined using the Chebyshev polynomials with 12 coefficients. An additional Gaussian peak was incorporated to the background to fit a broad peak at around 1.4 $Å^{-1}$ due to a Kapton capillary. Table S1, Fig. S1, and Table S2 show the refinement details, the result of the profile fitting, and the refined structural parameters, respectively. Although no secondary phase was detected by the present measurement, there might exist small amount of Mg or MgO (due to native surface oxide of starting material powder) with low crystallinity. We could not detect signs of excess Mg occupied at interstitial sites in the crystal structure.

Table S1 Crystal data, condition of data collection, and refinement results.

Crystal data	
Formula, Z	$Mg_3Sb_{1.5}Bi_{0.49}Te_{0.01}$, $Z = 1$
Symmetry, Space group	Trigonal, $P\bar{3}m1$
Unit cell parameters	$a = b = 4.58316(8)$ Å, $c = 7.27282(8)$ Å
	$\alpha = \beta = 90°$, $\gamma = 120°$
Volume	132.301(3) $Å^3$
Density	4.50879(10) g/cm^3
Condition of data collection	
Beamline	Advanced Photon Source (APS) 11-BM
Specimen mounting	0.8 mm dia. Kapton capillary
Collection mode	Transmission
Wavelength	0.414537 Å
Collection range	$0.5° < 2\theta < 49.997°$
Analysis range	$2.5° < 2\theta < 40°$ (0.66 $Å^{-1} < q < 10.37$ $Å^{-1}$)
Refinement results	
Number of data points	37559
Number of refined parameters	28
Number of refined reflection	273
R_{wp}	7.15%
R_p	5.57%
R_F	1.68%

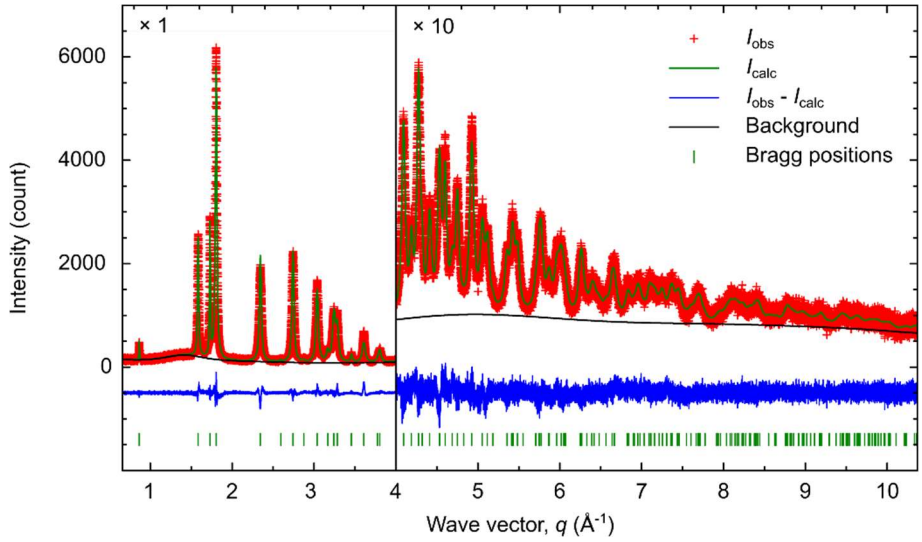

Fig. S1 Result of the Rietveld refinement.

Table S2 Structural parameters. In the refinement, all the occupancy parameters were fixed to be $Mg_3Sb_{1.5}Bi_{0.49}Te_{0.01}$. The fractional coordinates (x, y, and z) and the isotropic atomic displacement parameters (U_{iso}) of Sb, Bi, and Te were constrained to be the same.

Atom	Site	Occupancy	x	y	z	U_{iso}
Mg(1)	1*a*	1	0	0	0	0.0350(10)
Mg(2)	2*d*	1	1/3	2/3	0.6313(2)	0.0137(4)
Sb	2*d*	0.75	1/3	2/3	0.22683(5)	0.01461(12)
Bi	2*d*	0.245	1/3	2/3	0.22683	0.01461
Te	2*d*	0.005	1/3	2/3	0.22683	0.01461

S2. Electron backscattering diffraction (EBSD) mapping

In general, EBSD mapping is a real-time graphical pattern matching process to index observed electron diffraction patterns (Fig. S2) using predefined unit cell parameters.[4] To obtain clear diffraction patterns, preparing a flat and clean surface is crucial. In this work, sintered samples were polished with abrasive papers, followed by Ar-beam milling (Leica EM TIC 3X; Germany). We used the unit cell parameters obtained by the structural refinement in S1. Figure S3 shows crystal orientation maps in a wide area and inverse pole figures of samples sintered at 873 K [Fig. S3(a) and S3(c)] and 1123 K [Fig. S3(b) and S3(d)], respectively. Randomly-scattered inverse pole figures indicate that the samples have no preferential orientation. With a rather simplified assumption that the grains are spherical, we computed the average grain size by multiplying a factor of $\sqrt{3/2}$ to the nominal diameter values obtained from Fig. S3(a) and S3(b).

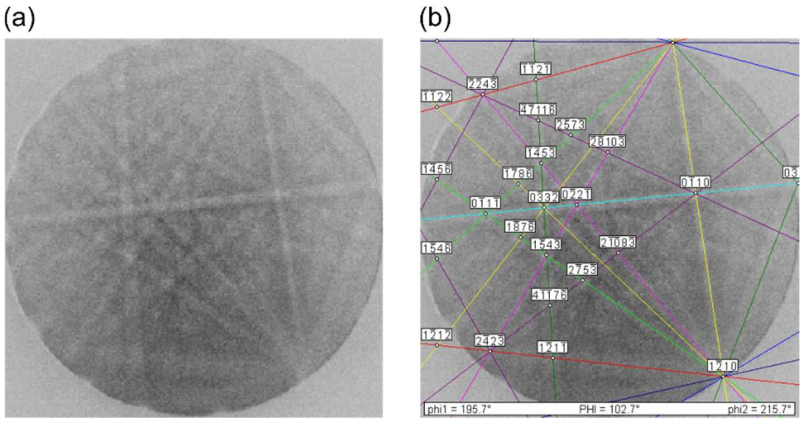

Fig. S2 (a) EBSD pattern (Kikuchi bands) of $Mg_{3.2}Sb_{1.5}Bi_{0.49}Te_{0.01}$ and (b) a result of indexing (using four-index notation for a trigonal unit cell). The acceleration voltage of electron beam was 15 kV, the tilt angle of the sample was 70°, and the working distance was 15 mm.

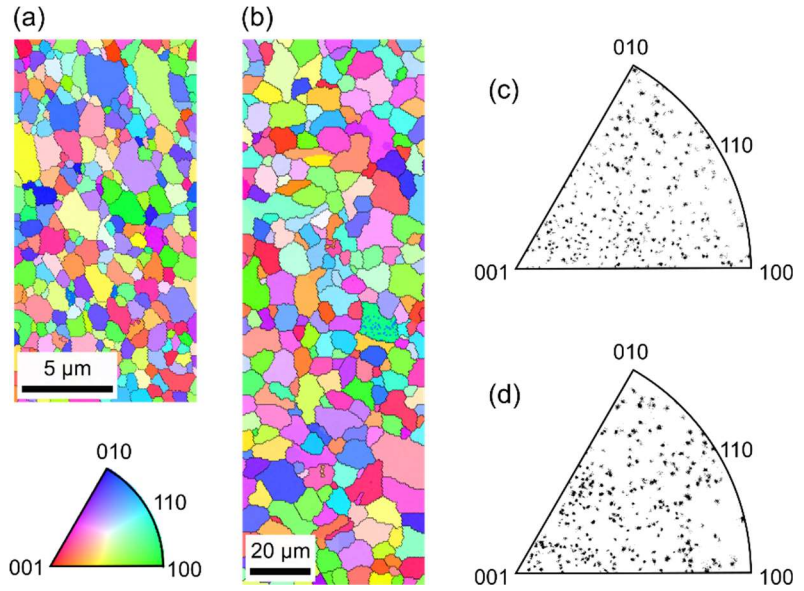

Fig. S3 (a) EBSD maps of samples sintered at 873 K and (b) 1123 K. (c) Inverse pole figure of samples sintered at 873 K and (d) 1123 K. The scanned area, the hexagonal pixel size, and the exposure time per pixel are (a) 20 μm × 10 μm, 0.1 μm, 0.16 sec, (b) 180 μm × 60 μm, 0.6 μm, and 0.14 sec.

S3. Chemical composition analysis

We performed composition analysis of samples sintered at 873 K and 1123 K with the nominal composition $Mg_{3.2}Sb_{1.5}Bi_{0.49}Te_{0.01}$ using energy-dispersive X-ray spectroscopy (EDS) and inductively coupled plasma atomic emission spectroscopy (ICP-AES) techniques. EDS measurement was performed using a scanning electron microscope (SU-8220, Hitachi High-Technologies; Japan) equipped with two kinds of EDS detectors: one was a standard silicon drift detector for quantitative analysis (Quantax XFlash 6|10, Bruker; Germany) and the other was an annular detector with the higher solid angle for fast EDS mapping (Quantax FlatQUAD, Bruker; Germany). Quantitative analysis of Mg, Sb, and Bi was conducted using measurements of 10 different points for each sample. The acceleration voltage was 10 kV and the collection time was 200 sec (~ 8 kcps) for each measurement. The PB-ZAF absorption correction was adopted. EDS mapping was performed with the acceleration voltage of 10 kV and the collection time was 600 sec (~ 350 kcps). The PB-ZAF absorption correction and background subtraction were also conducted for mapping. For ICP-AES analysis, content of Te and possible contamination of Fe during the ball-milling process was also checked.

Table S3 show the results of composition analysis with different techniques. The measured composition values were confirmed to be the same as the nominal composition within a few percent, which is comparable to the measurement errors of EDS or ICP-AES.

Figure S4 shows a result of EDS mapping of a sample sintered at 1123 K. No noticeable variations in the composition were found, and the sample was homogeneous in the observed length scale.

Table S3 Results of composition analysis. Sum of atomic composition of Sb and Bi is fixed to be 1.99.

Nominal composition	Sintering temperature	Analysis	Mg	Sb	Bi	Te	Fe
$Mg_{3.2}Sb_{1.5}Bi_{0.49}Te_{0.01}$	1123 K	ICP-AES	3.22	1.52	0.47	0.01	< 0.001
		EDS	3.21	1.54	0.45	–	–
	873 K	ICP-AES	3.22	1.50	0.49	0.01	< 0.001
		EDS	3.30	1.52	0.47	–	–

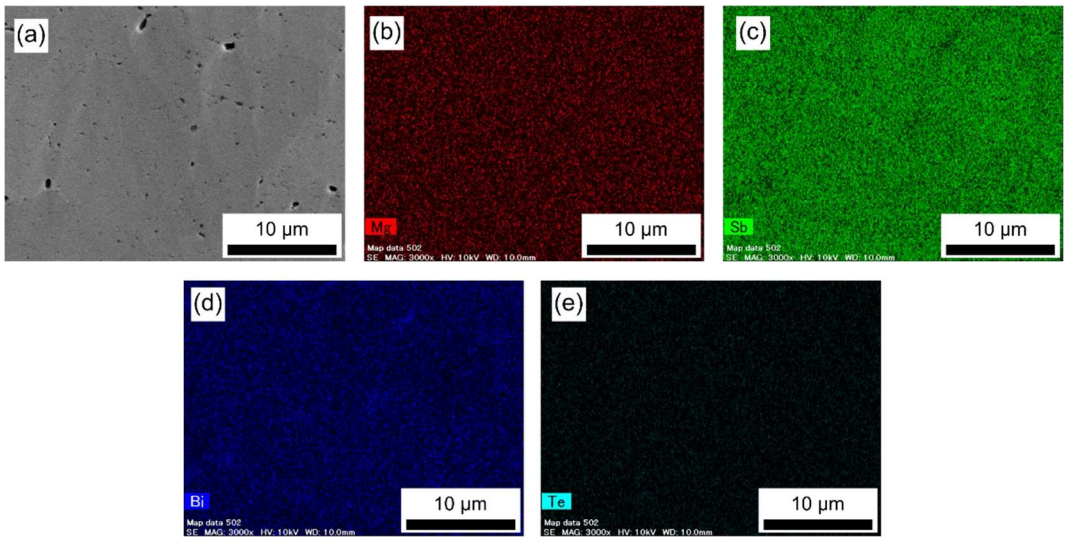

Fig. S4 EDS maps. (a) Secondary electron image. Elemental distributions of (b) Mg, (c) Sb, (d) Bi, and (e) Te.

S4. Thermal stability

We performed the thermogravimetric-differential scanning calorimetry (TG-DSC, Netzsch STA449 F1 Jupiter; Germany) measurement of $Mg_{3.2}Sb_{1.5}Bi_{0.49}Te_{0.01}$ bulk samples sintered at 1123 K and cut into approximately 3 × 2 × 1 mm^3. Figure S5(a) shows TG-DSC data under a constant heating rate of 20 K/min in Ar or air atmosphere. In Ar, no mass change was observed while a broad exothermic peak around 900 K and an endothermic peak at 1123 K were observed. The exothermic peak is possibly due to relaxation of residual strain in a sample prepared by SPS. The endothermic reaction at 1123 K corresponds to the structural phase transition from α-phase (trigonal $P\bar{3}m1$) to β-phase (cubic $Ia3$).[5-8] In air, immediate continuous oxidation started at around 1000 K (0.5% mass increase occurred at 977 K).

Figure S5(b) shows TG-DSC data under the constant temperature of 673 K or 773 K in air. At 673 K, no mass change was observed for 24 h. On the other hand, at 773 K, mass increase due to continuous oxidation started after approximately 10 h (0.5% mass increase occurred at 10.8 h).

To estimate the thermal stability of the sintered $Mg_{3.2}Sb_{1.5}Bi_{0.49}Te_{0.01}$ sample in high temperature air, we assume the Arrhenius law $t(T) = A\exp(E_a/k_BT)$ holds for the lifetime $t(T)$ of the sample in terms of oxidation failure. Here, A is a constant, E_a is the activation energy, and k_B is the Boltzmann constant. If we assume that the continuous oxidation started 1 min before (at 957 K) the mass increase of 0.5% occurred at 977 K [Fig. S5(a)], the activation energy E_a and the constant A are 2.2 eV and 1.6 × 10^{-12} min, respectively. The lifetime at 720 K is estimated to be 1.3 × 10^2 h. Although $Mg_{3.2}Sb_{1.5}Bi_{0.49}Te_{0.01}$ is relatively stable against oxidizing atmosphere, a protective coating or encapsulation is needed to operate this material in the most efficient temperature condition for a long time.

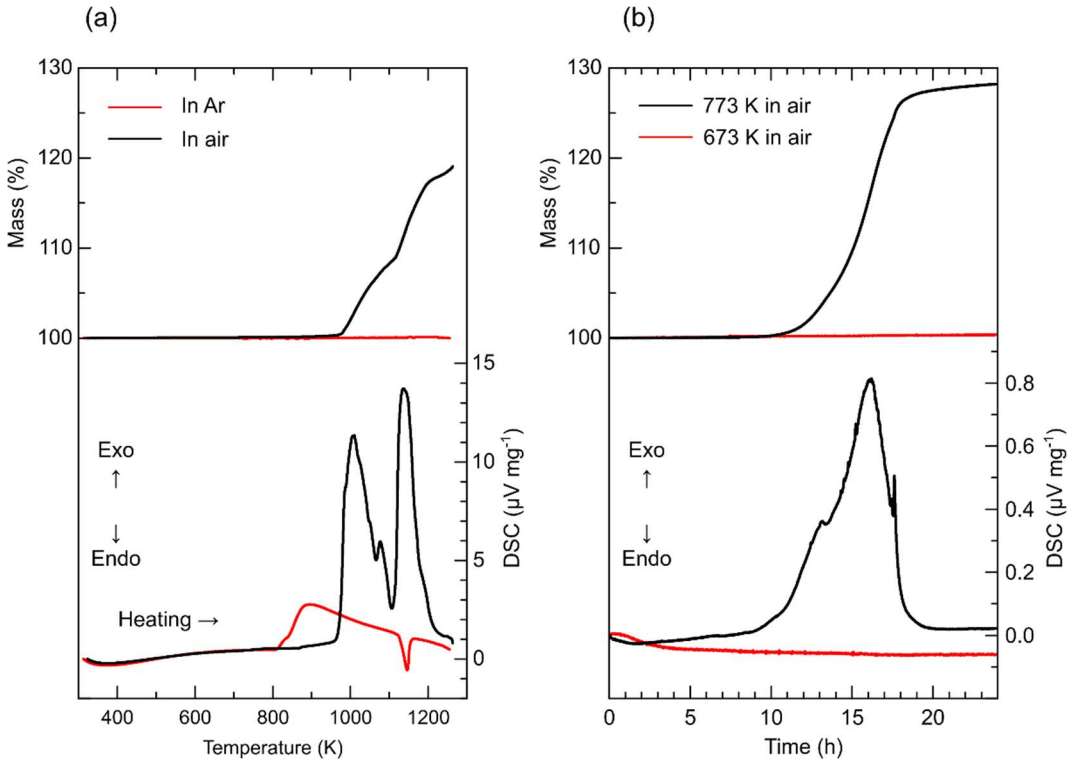

Fig. S5 TG-DSC data of $Mg_{3.2}Sb_{1.5}Bi_{0.49}Te_{0.01}$ bulk samples (a) under a constant heating rate of 20 K/min in Ar or air atmosphere, and (b) under the constant temperature of 673 K or 773 K in air.

References

1. B. H. Toby and R. B. Von Dreele, "GSAS-II: The genesis of a modern open-source all purpose crystallography software package", J. Appl. Cryst. **46**, 544 (2013).
2. Thompson, D. E. Cox, and J. B. Hastings, "Rietveld refinement of Debye-Scherrer synchrotron X-ray data from Al_2O_3", J. Appl. Cryst. **20**, 79 (1987).
3. W. Stephens, "Phenomenological model of anisotropic peak broadening in powder diffraction", J. Appl. Cryst. **32**, 281 (1999).
4. F.J. Humphreys, "Review Grain and subgrain characterisation by electron backscatter diffraction" J. Mater. Sci. **36**, 3833 (2001).
5. E. Zintl and E. Husemann, "Bindungsart und Gitterbau binärer Magnesiumverbindungen", Z Phys. Chem. **21B**(1), 138 (1933).
6. M. Martinez-Ripoll, A. Haase, and G. Brauer, "The crystal structure of α-Mg_3Sb_2". Acta Cryst. B **30**, 2006 (1974).
7. A. A. Nayeb-Hashemi and J. B. Clark, "The Mg−Sb (Magnesium-Antimony) system", Bull. Alloy Phase Diagr. **5**, 579–584 (1984).
8. A. A. Nayeb-Hashemi and J. B. Clark, "The Bi-Mg (Bismuth-Magnesium) system", Bull. Alloy Phase Diagr. **6**, 528 (1985).